TU Delft

Delft University of Technology

Analyzing the PN junction impedance of crystalline silicon solar cells across varied illumination and temperature conditions

van Nijen, David A.; Naoom, Salem; Muttillo, Mirco; Procel, Paul; Zeman, Miro; Isabella, Olindo; Manganiello, Patrizio

DOI
10.1016/j.solmat.2024.113255

Publication date
2025

Document Version
Final published version

Published in
Solar Energy Materials and Solar Cells

Citation (APA)
van Nijen, D. A., Naoom, S., Muttillo, M., Procel, P., Zeman, M., Isabella, O., & Manganiello, P. (2025). Analyzing the PN junction impedance of crystalline silicon solar cells across varied illumination and temperature conditions. *Solar Energy Materials and Solar Cells*, *279*, Article 113255. https://doi.org/10.1016/j.solmat.2024.113255

Important note
To cite this publication, please use the final published version (if applicable).
Please check the document version above.

Copyright
Other than for strictly personal use, it is not permitted to download, forward or distribute the text or part of it, without the consent of the author(s) and/or copyright holder(s), unless the work is under an open content license such as Creative Commons.

Takedown policy
Please contact us and provide details if you believe this document breaches copyrights.
We will remove access to the work immediately and investigate your claim.

This work is downloaded from Delft University of Technology.
For technical reasons the number of authors shown on this cover page is limited to a maximum of 10.

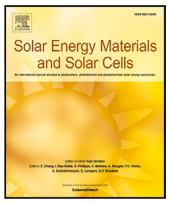
Solar Energy Materials & Solar Cells 279 (2025) 113255



Contents lists available at ScienceDirect

Solar Energy Materials and Solar Cells

journal homepage: www.elsevier.com/locate/solmat



Analyzing the PN junction impedance of crystalline silicon solar cells across varied illumination and temperature conditions

David A. van Nijen *, Salem Naoom, Mirco Muttillo, Paul Procel, Miro Zeman, Olindo Isabella *, Patrizio Manganiello

Delft University of Technology, Mekelweg 4, Delft, 2628 CD, The Netherlands

ARTICLE INFO

Dataset link: https://doi.org/10.4121/5b387cd1-9b99-4042-a7b5-e92f5ad198a4

Keywords:
Photovoltatronics
Capacitance
Impedance
Impedance spectroscopy
PN junction
Crystalline silicon

ABSTRACT

The impedance of solar cells can be leveraged for a variety of innovative applications. However, for the continued advancement of such applications, it is crucial to understand how the impedance varies during practical operation. This work characterizes the impedance of modern crystalline silicon solar cells across different bias voltages and under varying illumination and temperature conditions. It is found that for a given bias voltage, variations in temperature have a notably stronger impact on PN junction impedance than changes in irradiance. However, during maximum power point (MPP) tracking, variations in irradiance have a larger influence on the PN junction impedance than temperature variations. This is related to the shifting operating voltage during operation. Furthermore, it is shown that the capacitance during practical operation can strongly vary for different solar cells. For instance, the areal MPP capacitance values of the two cells tested in this study at 0.1 sun irradiance and a temperature of 30 °C were 0.283 μF/cm^2 and 20.2 μF/cm^2, a 71-fold difference. Conversely, the range of the MPP diffusion resistance was found to be highly similar for different cells. The results of this study enhance the understanding of solar-cell impedance and have a broad applicability.

1. Introduction

In photovoltaic (PV) systems, the main purpose of solar cells is to produce a direct current (DC) upon exposure to sunlight. Much of the research and development in solar energy focuses on enhancing the efficiency of solar cells in converting light into electrical power. However, the potential use of solar cells for high-frequency alternating current (AC) applications makes it valuable to explore and refine their impedance. For instance, studying the solar-cell impedance can rapidly gather large amounts of data for efficient and accurate measurements of a variety of solar cell parameters [1–3]. Additionally, the solar-cell impedance influences the performance of power electronics that perform maximum power point tracking (MPPT). To achieve a high performance in such power conditioning circuits, it is important that the converter is designed in accordance with the solar-cell impedance at the input [4]. Taking this one step further, it has been proposed to exploit the self-impedance of solar cells, which could lead to the development of converters that require fewer passive components at the input [5,6]. In a somewhat similar application, it has been reported that the solar cell self-capacitance can be used for power balancing among different cells [7]. Moreover, the impedance of solar cells impacts their suitability for applications beyond energy generation, such as Visible Light Communication (VLC) systems. In such systems, where solar cells can be simultaneously employed as power sources and receivers [8–10], the impedance directly influences the system's bandwidth [11]. These examples highlight the potential of solar-cell impedance analysis to reveal intrinsic device characteristics and pave the way for innovations.

Several studies have been published on the impedance of crystalline silicon (c-Si) solar cells. For instance, by analyzing the dynamics of direct and reverse *I–V* measurements with a pulsed solar simulator, maximum power point capacitance values under STC conditions have been reported for various commercial PV modules [12]. Subsequently, the authors report the "effective capacitance" at the maximum power point (MPP), which varies between 2.9 μF/cm^2 and 108 μF/cm^2 for the different cells. However, this publication does not take into account different illumination intensities and frequency-dependent effects. Furthermore, an impedance spectroscopy analysis has compared the impedance of various modern commercial solar cells in dark conditions. There, areal MPP capacitance values between 0.30 and 45.6 μF/cm^2 are found for the different cells. Additionally, there are numerous publications employing impedance spectroscopy to reveal underlying solar-cell characteristics [13–23]. Moreover, several reports focus on fault detection, performing impedance spectroscopy on larger cells and modules [24–28].

* Corresponding authors.
E-mail addresses: d.a.vannijen@tudelft.nl (D.A. van Nijen), o.isabella@tudelft.nl (O. Isabella).

https://doi.org/10.1016/j.solmat.2024.113255
Received 17 July 2024; Received in revised form 26 September 2024; Accepted 24 October 2024
Available online 5 November 2024
0927-0248/© 2024 The Authors. Published by Elsevier B.V. This is an open access article under the CC BY license (http://creativecommons.org/licenses/by/4.0/).

Nevertheless, in the pursuit of exploiting the solar-cell impedance in the applications that were mentioned earlier, it is important to understand how the impedance of the solar cell varies during operation. For instance, when solar cells are deployed in real-world conditions, they are subjected to varying levels of irradiance and temperature. To compensate for these environmental changes, MPPT is employed, which continually adjusts the operating voltage of the solar cell. This dynamic interaction of multiple factors leads to fluctuations in the impedance during practical operation. It is expected that there may be some variation in series resistance during operation [2,17,29], whereas the changes in the inductance would be limited [30,31]. However, the PN junction impedance dominates the overall impedance at low frequency and is anticipated to show the highest variability with changes in bias voltage, irradiance, and temperature. Additionally, the greatest knowledge gap relates to a quantification of the variability of the PN junction impedance.

Consequently, the primary objective of this study is to understand how the PN junction impedance of modern c-Si solar cells varies under real-world operating conditions. Impedance data are gathered through both experimental impedance spectroscopy and Technology Computer-Aided Design (TCAD) simulations. The experimental part of the study is performed using single-cell laminates based on commercial Passivated Emitter and Rear Contact (PERC) and interdigitated-back-contact (IBC) solar cells. The TCAD part is conducted using a Tunnel Oxide Passivated Contact (TOPCon) solar cell architecture with efficiency approaching the performance limit of c-Si cells. It is worth noting that the architecture of a solar cell (e.g., aluminum back surface field, PERC, silicon heterojunction, TOPCon, IBC) has little influence on the capacitance–voltage (C–V) relationship. Instead, the C–V relationship is primarily affected by the substrate dopant concentration (N_{sub}), also known as the wafer or bulk dopant concentration [32]. Specifically, a low N_{sub} leads to high capacitance in forward bias. Moreover, a highly efficient cell likely has a high maximum power point voltage (V_{mpp}), which in turn leads to an increased capacitance during operation. By experimentally examining the impedance of cells with different values of N_{sub} and V_{mpp}, we gain insights into the variations among modern commercial c-Si solar cells. Moreover, the TCAD simulations provide insights into the behavior of solar cells approaching the efficiency limit.

The paper is structured as follows: The method is detailed in Section 2; In Section 3, the small-signal equivalent modeling of solar-cell impedance is discussed, along with discussions on the limitations of the employed model; Section 4 presents the results and discussion; Finally, the conclusions are given in Section 5.

2. Method

2.1. Experimental impedance characterization

For the experimental part of this study, two single-cell laminates based on commercial c-Si solar cells were fabricated. The first laminate was based on an interdigitated-back-contact (IBC) solar cell laminated in a stack consisting of glass - EVA (ethylene vinyl acetate) - cell - EVA - backsheet. The second laminate was based on a PERC solar cell laminated in a stack consisting of glass - TPO (thermoplastic polyolefin) - cell - TPO - backsheet. For both laminates the standard test conditions (STC) parameters are presented in Table 1, along with the series resistance (R_s), shunt resistance (R_{sh}), cell area, substrate dopant concentration (N_{sub}), and built-in potential (V_{bi}). These specific cells were selected because the PERC cell has a high N_{sub} and low V_{mpp}, whereas the IBC cell has a low N_{sub} and high V_{mpp}. Therefore, the operational capacitance of these cells is expected to be around the lower and upper limits that can be anticipated from modern commercial c-Si solar cells.

For the experimental impedance characterization of this study, an in-house developed impedance spectroscopy setup is employed. During the impedance recordings, the cell is biased at a certain direct current (DC) operating point, after which a small-signal alternating current (AC) voltage is superimposed. The resulting AC waveforms of the voltage and current signals are analyzed using lock-in amplifiers. The employed setup is similar to one reported in a previous publication [32], but includes some modifications:

- A controllable LED-based light source with an AM1.5-like spectrum in the visible range is fixed above the solar laminate, allowing to set the irradiance.
- During the measurements, the laminate is placed on an 80 cm × 80 cm temperature-controlled plate, enabling temperature regulation. The laminate temperature is monitored using a thermocouple and a Pico logger. In the case of the PERC laminate, the thermocouple is directly attached to the back of the solar cell and included in the lamination stack. In the case of the IBC laminate, the thermocouple is attached to the backsheet of the laminate.
- Similar to previous work [32], the output of an OPA-549 op-amp, configured as a non-inverting summing amplifier, is connected at the positive contact of the solar cell. However, unlike the direct connection of the negative contact of the solar cell to the ground in prior work, in this study, we connect the negative contact to the negative terminal of a second OPA-549 op-amp. This configuration ensures compatibility with the utilized unidirectional power supply when a photocurrent arises in the solar cell.

A schematic representation of the employed impedance spectroscopy setup is shown in Fig. 8 of Appendix A. Throughout this study, all reported experimental impedance measurements are conducted once the solar-cell temperature stabilizes at the desired level. The temperature is varied from 30 °C to 60 °C, while the irradiance ranges from dark conditions to 0.5 sun. The reported frequency range for the experimental impedance data spans from 5 Hz to 10 kHz.

Table 1
Properties of the single-cell laminates employed in this study. The efficiency, the open-circuit voltage (V_{OC}), the short-circuit current density (J_{SC}), the fill factor (FF), and the maximum power point voltage (V_{mpp}) are all obtained in STC conditions using a LOANA solar cell analysis system [33]. The R_s is the global series resistance, which is found from comparing the J_{SC}–V_{OC} measurement with light-IV [33]. The R_{sh} is approximated by taking the inverse slope of the dark IV curve at 25 °C, using data between −25 mV and +25 mV. Finally, N_{sub} and V_{bi} are extracted in dark conditions according to the methodology presented in a previous publication [32].

	IBC	PERC
Efficiency (%)	23.75	18.46
V_{OC} (V)	725.0	649.6
J_{SC} (mA/cm^2)	40.49	36.47
FF (–)	0.809	0.779
V_{mpp} (V)	622	534
R_s (Ω cm^2)	0.69	0.69
R_{sh} (Ω cm^2)	1.02×10^4	2.90×10^4
Cell area (cm^2)	153	122.15
N_{sub} (atoms × cm^{-3})	1.0×10^{14}	8.0×10^{15}
V_{bi} (mV)	0.58	0.63

2.2. TCAD impedance simulations

Furthermore, as solar cells get closer to the performance limit in the coming years, their impedance may change. To investigate this, a performance-limit c-Si device is studied by using the finite element simulator TCAD Sentaurus [34]. A TOPCon architecture was selected, as this is predicted to become the dominant cell concept in terms of market share by 2024 [35]. Specifically, the simulated cell structure is a specific type of TOPCon architecture known as the PeRFeCT (Passivated Rear and Front ConTacts) solar cell [36]. This device architecture features: (i) a highly transparent lightly P-doped homojunction as front surface field (FSF); (ii) a P-doped TOPCon layer formed only underneath the front metal grid; (iii) a rear emitter with a B-doped poly-Si layer deposited on thin SiO_x. While utilizing the

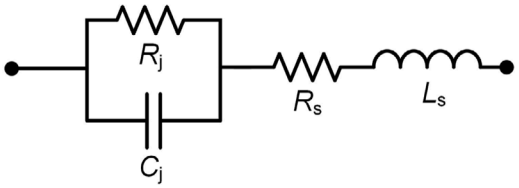


Fig. 1. Solar cell small-signal circuit that is employed in this study for equivalent model fitting.

PeRFeCT device architecture, the device parameters are adjusted to approach the performance limit of c-Si devices, similar to a previous publication [37]. Regarding the structure, the wafer thickness is 200 μm and the front side metallization coverage is 0.833% with a finger width of 5.0 μm. At $N_{sub} = 3.2 \times 10^{15}$ cm^{-3}, the simulated efficiency under STC reaches 26.9%, with an open-circuit voltage of 739 mV, a short-circuit current density 43.4 mA/cm^2, a fill factor of 0.841, and a maximum power point voltage of 649 mV. It is worth noting that the TCAD solar cell structure does not account for the non-idealities that can reduce shunt resistance in practical devices, of which an overview is given in previous work [38]. As a result, the shunt resistance in the simulated device is higher than what is typically expected in practical solar cells, and the current near zero bias voltage is primarily governed by recombination and generation currents [39]. Despite this, the slope and shape of the *I–V* curve in forward bias remain realistic for practical devices.

The small-signal AC analysis is conducted using the *ACCoupled* solve section of TCAD Sentaurus. This simulation generates a frequency-dependent impedance matrix, comprising the real and imaginary parts of the impedance at each frequency examined during the AC analysis. In this study, the reported frequency range spans from 1 nHz to 1 MHz. The temperature is varied from 15 °C to 75 °C, while the irradiance ranges from dark conditions to 1.2 suns.

2.3. Small-signal equivalent circuit fitting

Fig. 1 shows the small-signal equivalent circuit that is used in this study to model the solar-cell impedance. The parallel resistor–capacitor circuit (*RC*-loop) represents the PN junction impedance. Here, C_j represents the PN junction capacitance, which is the parallel combination of depletion capacitance and diffusion capacitance, with equations provided in Appendix B. Additionally, R_j represents the PN junction resistance, which is the parallel combination of the diffusion resistance and the shunt resistance. In practical devices, R_j is primarily governed by the shunt resistance near zero bias, but by the diffusion resistance at forward bias voltages. Moreover, the circuit in Fig. 1 includes a series resistance R_s and an inductance L_s. While this model generally gives an effective representation of the solar-cell impedance, it is worth noting that it does not account for certain high-frequency phenomena related to the minority carrier diffusion. These limitations are further discussed in Section 3.

The impedance of the circuit in Fig. 1 is given by the following equation:

$$Z = i\omega L_s + R_s + \left[R_j \parallel \frac{1}{i\omega C_j} \right] \tag{1}$$

where i denotes the imaginary unit. Eq. (1) can be rewritten into the form $Z = Z' + iZ''$ with the real part Z' and the imaginary part Z'' being defined as follows:

$$Z' = R_s + \frac{R_j}{1 + R_j^2\omega^2 C_j^2} \tag{2}$$

$$Z'' = \omega L_s - \frac{R_j^2\omega C_j}{1 + R_j^2\omega^2 C_j^2} \tag{3}$$

To determine the values of the circuit parameters in Fig. 1 at any bias voltage V_{DC}, Eqs. (2) and (3) are simultaneously fitted to the recorded impedance data through complex nonlinear least-squares (CNLS) analysis [40]. For the fitting procedure, the MATLAB *lsqcurvefit* solver is used, with the fitting parameters being C_j, R_j, L_s, and R_s.

3. Impedance modeling considerations

3.1. High-frequency R_j and C_j relaxation

There are typically two junctions present in c-Si solar cells, which are the PN junction and the low-high (LH) junction. It is widely acknowledged that the impedance of a PN junction can be modeled using a parallel resistor–capacitor circuit (*RC*-loop) [39]. Additionally, in studies on solar-cell impedance, the LH junction is often accounted for by incorporating into the equivalent circuit an additional *RC*-loop in series with the PN-junction *RC*-loop [2,4,17,19,26,32]. In recent publications on TOPCon and silicon heterojunction cells, a constant phase element (CPE) or a third *RC*-loop is even introduced to solar-cell impedance models to address various non-ideal effects in such devices [21,22]. While good fitting quality can be achieved, linking the elements in these advanced equivalent circuits to the underlying physics remains challenging. For instance, a recent publication has demonstrated that the approach of modeling the LH junction with an *RC*-circuit may not accurately represent the underlying physics [41]. Instead, it was shown that the inclusion of a second *RC*-loop may account for the relaxation of R_j and C_j with frequency. It is worth noting that the relaxing behavior of R_j and C_j sometimes manifests in the impedance in a manner closely resembling the impedance of two *RC*-loops. Depending on the solar cell under study and its operating conditions, the modeling approach based on two series-connected *RC*-loops may still yield accurate fitting results.

3.2. Model accuracy at different bias voltages

This section elaborates on when and how the relaxation of R_j and C_j manifests in the impedance of a solar cell. Fig. 2 illustrates TCAD-generated impedance spectra of the TOPCon solar cell that was introduced in Section 2.2. The area of the cell is set to 153 cm^2, and the impedance is presented at bias voltages of 0 mV, 400 mV, and 650 mV. For each voltage, the real part (Z'), imaginary part (Z''), magnitude, and phase of the impedance are depicted as functions of frequency. Additionally, each plot includes the optimal CNLS fit using the circuit from Fig. 1. It is important to note that a series resistance of $R_s = 5$ mΩ and an inductance of $L_s = 60$ nH, which are realistic values for the metal contacts in commercial solar cells [32], have been added to the TCAD-generated impedance data in Fig. 2. This adjustment ensures that the analysis does not overly emphasize impedance trends that would not be detectable in real-world devices. Additionally, the Nyquist spectra corresponding to Fig. 2 are presented in Fig. 9 of Appendix C.

In Fig. 2(a) at a bias voltage of $V_{DC} = 0$ mV, it is evident that the model gives an accurate fit, which is consistent with previous research [32]. However, as depicted in Fig. 2(b) at $V_{DC} = 400$ mV, it is apparent that the employed small-signal equivalent circuit fails to fully capture the impedance. While the fitting quality is high in the low-frequency range up to about 100 Hz, a deviation becomes noticeable for Z' at higher frequencies. It is worth noting that this deviation may remain obscured in a Nyquist spectrum on a linear scale, as shown in Fig. 9. The high-frequency behavior is likely related to the relaxation of R_j and C_j [41], and is also sometimes referred to as Warburg behavior [1]. At $V_{DC} = 650$ mV, as shown in Fig. 2(c), the same high-frequency relaxation phenomenon occurs. However, in this case it occurs at a frequency where Z' is already dominated by the series resistance (R_s). Consequently, the overall fit is considerably improved at 650 mV compared to 400 mV. In general, if the frequency at which Z' starts to be dominated by R_s is low enough, as seen

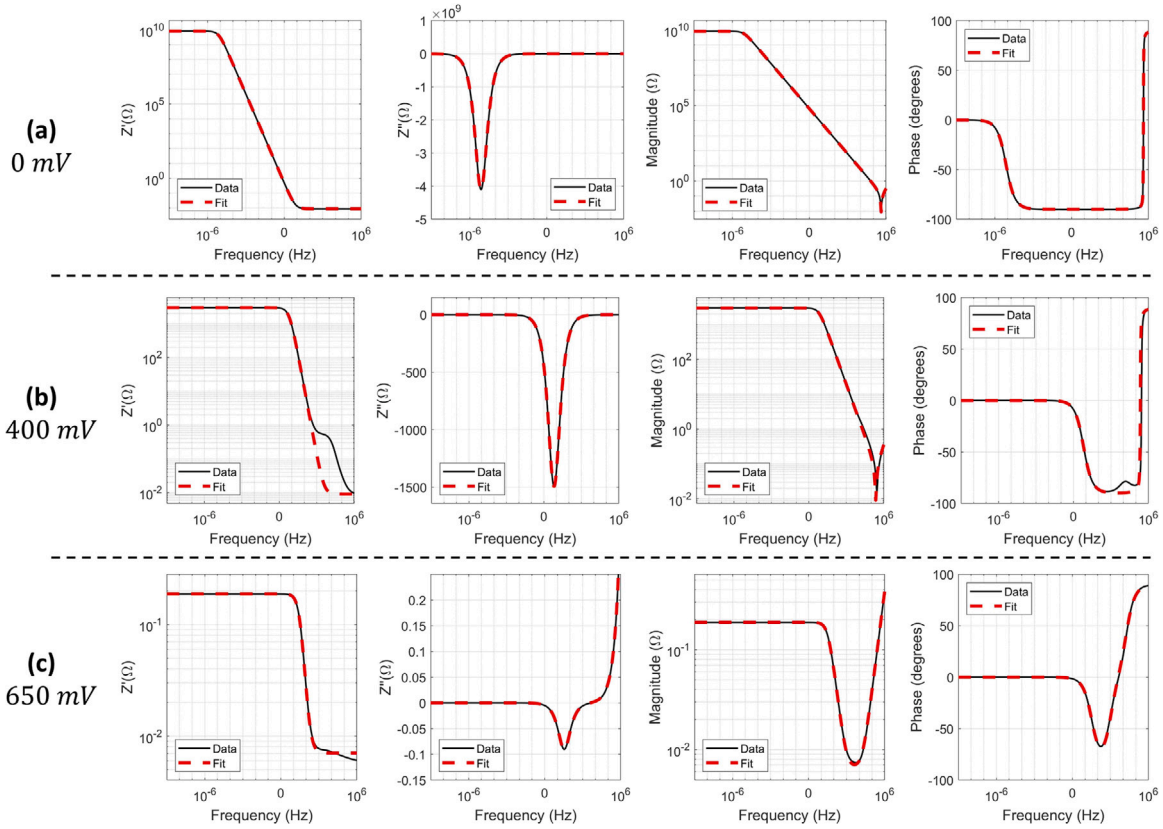


Fig. 2. TCAD-generated impedance data of TOPCon solar cell with an area of 153 cm^2, along with best CNLS fits at (a) 0 mV bias, (b) 400 mV bias, and (c) 650 mV bias. For each bias voltage, the plots display (from left to right) the real part (Z'), imaginary part (Z''), magnitude, and phase of the impedance. The bulk dopant concentration of the simulated solar cell is $N_{sub} = 3.2 \times 10^{15}$ cm^{-3} and the impedance data is simulated in dark conditions at a temperature of $T = 25$ °C.

in Fig. 2(a) and 2(c), the model yields accurate fits. However, if the relaxation of R_j and C_j occurs at a frequency lower than the point where Z' becomes dominated by R_s, as shown in Fig. 2(b), a deviation may occur between the fit and the actual impedance. Finally, it is worth mentioning that the data presented in Fig. 2 has little to no noise, since it is generated through TCAD simulations. When some noise is present during an experimental measurement, it can become more challenging to detect the relaxation of R_j and C_j.

3.3. Impedance modeling in practice

In the previous section, it was shown that in the bias voltage range above 0 mV and below the MPP voltage (V_{mpp}), the fit can deviate somewhat at high frequencies. However, since the fitting accuracy is high at low frequencies, the low-frequency values of R_j and C_j are still well identified by the employed procedure. Furthermore, when the tested solar cells are biased around their V_{mpp}, the small-signal equivalent circuit of Fig. 1 yields satisfactory fitting quality. To illustrate this, the impedance data of the different solar cells from this study are presented along with the CNLS fits in Fig. 3. Specifically, the impedance data are recorded at the V_{mpp} of each cell at 0.5 sun irradiance and a temperature of 30 °C. Fig. 3(a) includes TCAD-generated impedance data of the TOPCon solar cell with an area of 153 cm^2 and an added series resistance of $R_s = 5$ mΩ and inductance of $L_s = 60$ nH. Additionally, Fig. 3(b) and 3(c) present experimentally recorded impedance data of the IBC and PERC solar cell, respectively. The achieved fitting accuracy in Fig. 3 confirms the validity of the employed small-signal equivalent circuit at MPP. Additionally, the Nyquist spectra corresponding to Fig. 3 are presented in Fig. 10 of Appendix C.

4. Results and discussion

4.1. Effect of illumination

This section analyzes the effect of illumination on the PN junction impedance in solar cells. Before presenting the results obtained in this study, it is useful to briefly review the state of the art on this topic. It is known that the additional majority carriers generated due to illumination affect the depletion region width [1]. In previous publications it is described how the depletion region width in short-circuit condition approximately changes due to illumination [42,43]. For instance, for the p-side of a given PN junction, this change is described by the following relationship [42]:

$$W_{sc,p} \approx \frac{W_{d,p}}{1 + \delta/2} \tag{4}$$

with $\delta = \Delta n / N_a$. Here, $W_{sc,p}$ represents the illuminated p-side depletion region width, $W_{d,p}$ denotes the dark p-side depletion region width, Δn is the additional electron density generated due to the illumination, and N_a signifies the acceptor concentration on the p-side of the junction. Since the value of δ is inversely related to N_a, illumination leads to a more pronounced reduction in the depletion region width for lower dopant concentrations. Additionally, it is important to consider that a change in irradiance alters the DC current flowing through the device. Consequently, the effective voltage drop over the series resistance changes when the irradiance level is adjusted. Thus, even if the applied bias voltage at the outer device terminals remains unchanged, the irradiance level affects the effective voltage drop over the PN junction. In fact, it has been suggested that the change in effective voltage drop is the only effect that illumination has on the PN junction impedance in

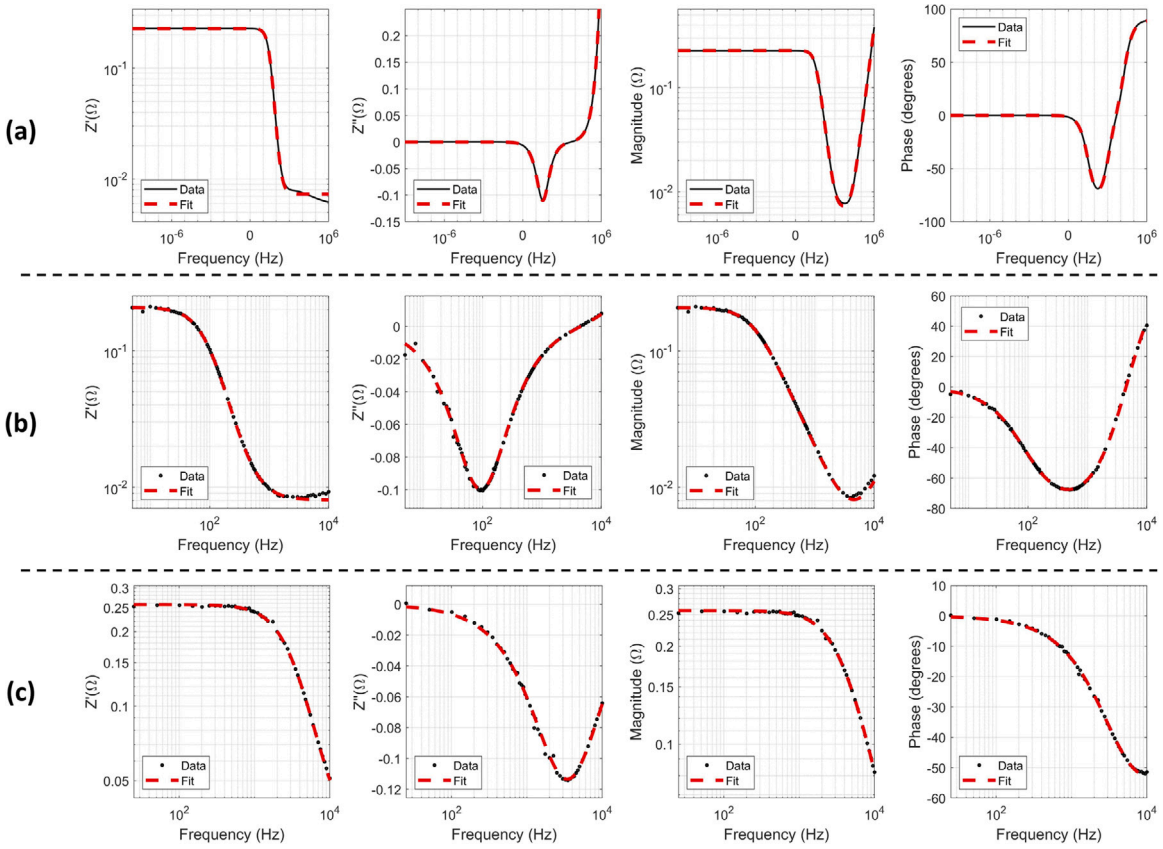


Fig. 3. Impedance at the maximum power point voltage with best CNLS fits for (a) the TCAD-generated impedance data of the TOPCon device with N_{sub} = 3.2 × 10^{15} cm^{-3}, (b) the experimentally recorded impedance data of the IBC solar cell laminate, and (c) the experimentally recorded impedance data of the PERC solar cell laminate. The plots display (from left to right) the real part (Z'), imaginary part (Z''), magnitude, and phase of the impedance. In all cases, the irradiance is 0.5 suns and the temperature is 30 °C.

solar cells [2]. To verify this, a useful feature of the TCAD approach can be utilized: the effective electrostatic potential across the PN junction (V_j) can be directly extracted. Therefore, the R_j and C_j values can be plotted as functions of the applied voltage on the outer terminals, as well as functions of the V_j.

In Fig. 4, the CNLS-fitted values of R_j and C_j are analyzed for the TCAD-simulated TOPCon device, across varying irradiance levels between dark conditions and 1.2 suns. Specifically, in Fig. 4(a) and Fig. 4(b), the R_j and C_j values are plotted as functions of the applied forward bias voltage, respectively. Moreover, the same R_j and C_j values are presented as functions of electrostatic PN junction potential (V_j) in Fig. 4(c) and Fig. 4(d), respectively. Furthermore, the corresponding results from the experimental part of this study are shown in Fig. 11 of Appendix D.

In Fig. 4(a), it is evident that at a given applied voltage, an increase in irradiance level lowers R_j. Comparing this to Fig. 4(c), it becomes apparent to what extent this effect is caused by an illumination-induced change in V_j. At low forward bias in Fig. 4(c), R_j decreases with increasing irradiance for a given V_j value. This is likely due to two main effects. Firstly, photogenerated charge carriers in the space charge region are swept out by the electric field, giving rise to a drift current. Secondly, at low forward bias, the forward-bias recombination current is often larger than the diffusion current [39]. The higher number of excess carriers in the space charge region under illumination increases the likelihood of recombination. Both these factors may be contributing to a reduction of R_j by increasing illumination at low forward bias. It is worth noting that these effects are much less, if at all, visible for the R_j values extracted from the experimental data presented in Fig. 11. In practical devices, the shunt resistance limits R_j around zero bias voltage. Consequently, the change in R_j at low bias voltage caused by illumination is less detectable from the experimental results. Furthermore, at forward bias (e.g., for $V_j > -0.45$ V), the R_j-V_j relationship of Fig. 4(c) remains nearly unaffected by illumination. This indicates that the effect that illumination has at high forward bias in Fig. 4(a) is mostly caused by a change in V_j. Furthermore, it is important to note that in deep forward bias (e.g., for $V_j > -0.2$ V), the slope of the R_j-V_j relationship in Fig. 4(c) changes. This change may be related to the bulk of the device no longer being in low-level injection conditions.

In Fig. 4(b), it is evident that for a given applied voltage, an increase in irradiance does increase C_j. This effect is most pronounced at a forward bias voltage between 0.4 V and 0.6 V. However, in Fig. 4(d), C_j is plotted as a function of V_j for different irradiance levels. In this case, the relationship remains nearly unaffected by illumination, indicating that the earlier changes in C_j due to illumination in Fig. 4(b) are mostly explained by a shift in V_j. This result is consistent with prior work [2]. Moreover, it is worth noting that the slope of the C_j-V relationship in Fig. 4(b) reduces at high forward bias (e.g., for V > 0.6 V), whereas the slope remains relatively constant for the C_j-V_j relationship in Fig. 4(d). This shows that the diminishing slope in Fig. 4(b) is predominantly caused by the applied voltage dropping across other parts of the device, such as the low-high junction and series resistance, rather than the PN junction. Finally, it is important to mention that at low bias voltage, the extent to which illumination affects C_j for a given applied voltage is strongly affected by the substrate dopant concentration. Indeed, from the experimental results presented in Fig. 11, it is evident that at low bias voltage, the C_j of the IBC device increases more strongly with illumination than that of the PERC device. This is presumably related to its significantly lower substrate dopant concentration, and consistent with the prediction from Eq. (4).

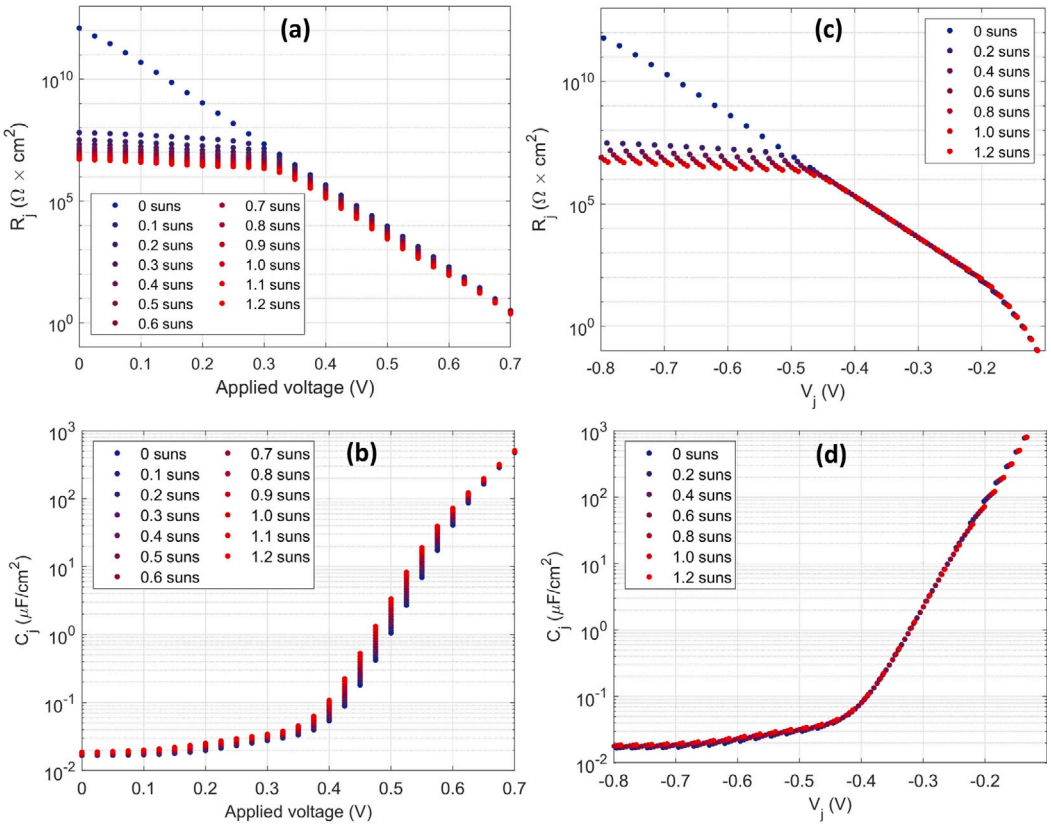


Fig. 4. Effect of illumination on R_j and C_j, as extracted from TCAD-generated impedance data of a TOPCon solar cell. The irradiance is varied between dark conditions and 1.2 suns in steps of 0.1 sun. (a) shows R_j and (b) shows C_j, both obtained through CNLS analysis and plotted as functions of applied forward bias voltage. Additionally, the same R_j and C_j values are presented as functions of V_j in (c) and (d). The bulk dopant concentration of the simulated solar cell is $N_{sub} = 3.2 \times 10^{15}$ cm^{-3} and the impedance data is simulated at a temperature of $T = 25$ °C.

4.2. Effect of temperature

This section analyzes the effect of temperature on the PN junction impedance in solar cells. Before presenting the results, it is useful to briefly review the relevant physics. An increase in the temperature of a semiconductor leads to a higher intrinsic carrier concentration, primarily due to an increase in the effective density of states in both the conduction and valence bands [39]. This higher carrier concentration increases the reverse saturation current density, implying that a higher temperature enhances diffusion across the depletion region. Moreover, similar to the previously discussed effect under illumination, the increased intrinsic carrier concentration at higher temperatures can reduce the depletion region width and hence the electrostatic junction potential V_j. Therefore, in the temperature analysis, it is useful to analyze the R_j and C_j values both as functions of the applied voltage on the outer terminals and as functions of V_j.

In Fig. 5, the CNLS-fitted values of R_j and C_j are analyzed for the TCAD-simulated TOPCon device, across varying temperature levels between 15 °C and 75 °C and under a fixed illumination of 0.5 sun. Specifically, in Fig. 5(a) and Fig. 5(b), the R_j and C_j values are plotted as functions of the applied forward bias voltage, respectively. Moreover, the same R_j and C_j values are presented as functions of V_j in Fig. 5(c) and Fig. 5(d), respectively. Furthermore, the corresponding results from the experimental part of this study are shown in Fig. 12 of Appendix D.

From Fig. 5(a), it is evident that a higher temperature leads to a lower R_j. However, the change is more prominent at high forward bias than at low forward bias. At low forward bias, the R_j of the TCAD-simulated device is primarily influenced by the forward-bias recombination current, which is at a relatively high level due to the presence of photogenerated charge carriers. Consequently, the changing temperature has a limited effect. At high forward bias, the R_j of the TCAD-simulated device is primarily influenced by the diffusion of minority carriers. Here, the higher temperature leads to enhanced diffusion, and in turn, a lower R_j. In Fig. 5(b), it can be seen that for low bias voltages, temperature has little effect on C_j. This is according to expectation, since the depletion capacitance dominates C_j in this regime. Conversely, in forward bias, a higher temperature clearly leads to a higher C_j at a given applied voltage. This is attributed to the enhanced diffusion capacitance. The TCAD results from Figs. 5(a) and 5(b) align with the experimental results shown in Fig. 12 of Appendix D, confirming these observations.

Additionally, when comparing Figs. 5(a) and 5(b) to Figs. 5(c) and 5(d), there are some subtle changes in the trends of R_j and C_j. Notably, the extent to which the temperature affects R_j and C_j for a fixed V_j value is somewhat less pronounced than for a fixed applied voltage. This indicates that part of the temperature effect observed in Figs. 5(a) and 5(b) is due to the narrowing of the depletion region width at higher temperatures. Moreover, when R_j and C_j are plotted as a function of V_j, it becomes apparent that the slopes become less steep as the temperature increases. This observation is consistent with theoretical expectations [39].

4.3. Impedance variations during MPPT

Now that the effects of illumination and temperature on the PN junction impedance have been thoroughly discussed, our focus shifts to impedance variations during practical operation. Here, one important factor must be included: the operating voltage is not constant. Fluctuations in irradiance and temperature affect the current–voltage (I–V)

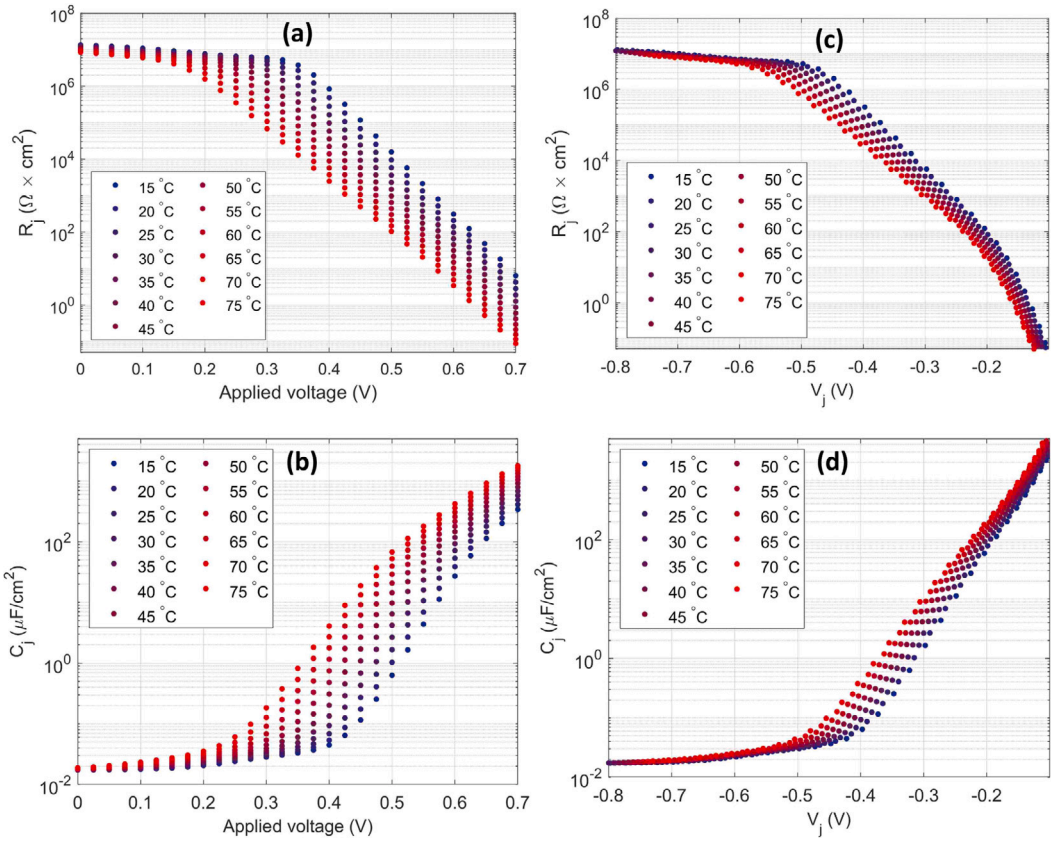


Fig. 5. Effect of temperature on R_j and C_j, as extracted from TCAD-generated impedance data of a TOPCon solar cell. The temperature is varied between 15 °C and 75 °C in steps of 5 °C. (a) shows R_j and (b) shows C_j, both obtained through CNLS analysis and plotted as functions of applied forward bias voltage. Additionally, the same R_j and C_j values are presented as functions of V_j in (c) and (d). The bulk dopant concentration of the solar cell is N_{sub}=3.2 × 10^{15} cm^{-3} and the impedance data is simulated under an irradiance of 0.5 sun.

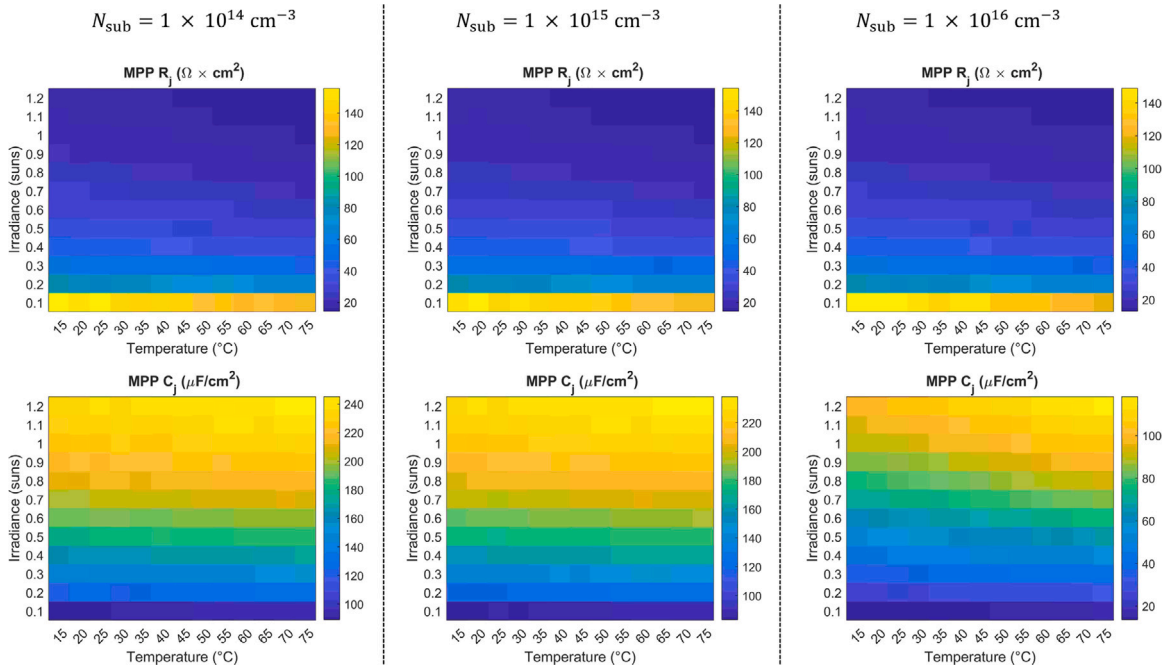


Fig. 6. Variation of R_j and C_j across varied irradiance and temperature conditions, with the DC bias voltage adjusted to the V_{mpp} corresponding to each condition. The values are obtained through CNLS fitting of TCAD-generated impedance data of TOPCon solar cells with different bulk dopant concentrations (N_{sub}).

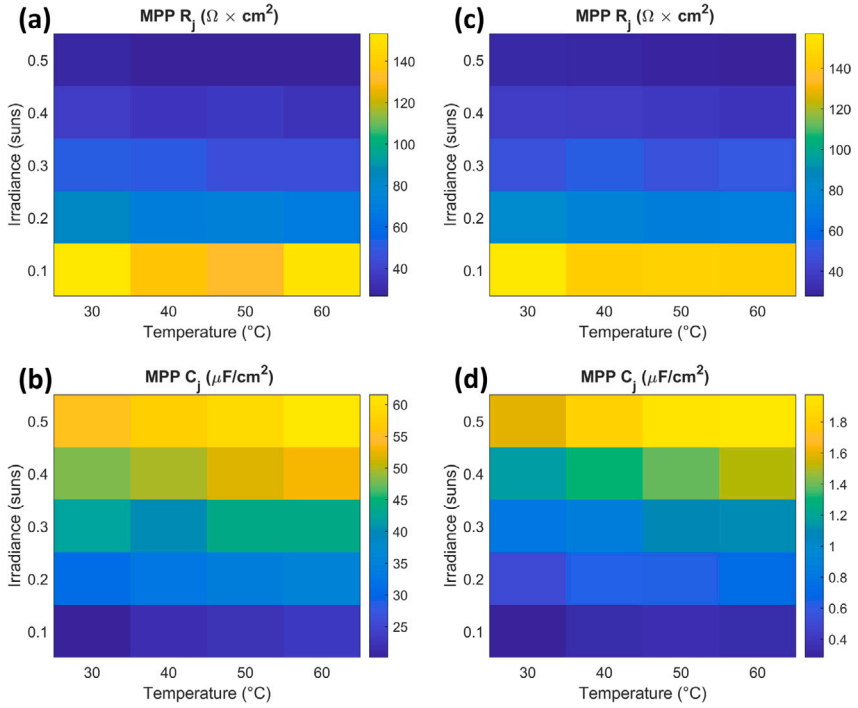


Fig. 7. Variation of R_j and C_j across varied irradiance and temperature conditions, with the DC bias voltage adjusted to the V_{mpp} corresponding to each condition. The values are obtained through CNLS fitting of experimentally recorded impedance data for the (a–b) IBC and (c–d) PERC solar cell laminates.

relationship. Thus, in practical PV systems, the maximum power point tracker (MPPT) continually adjusts the DC operating voltage to generate the maximum power. When irradiance increases, the maximum power point voltage (V_{mpp}) of the solar cell will increase as well. Thus, although the direct effect of illumination on the C_j-V relationship is limited, an increase in irradiance in real-world conditions will increase the operating voltage, in turn leading to a decreased R_j and an increased C_j. When it comes to temperature, the dynamics are different. As discussed in Section 4.2, a rising temperature will decrease R_j and increase C_j at a given voltage. However, an increase in temperature is known to lower the V_{mpp}. In turn, the lower operating voltage leads to a counterbalancing increase in R_j and decrease in C_j. In this section, the combined effects of the factors discussed above on the impedance variations are quantified.

First, the TCAD approach is used to study the variations in operating impedance of the TOPCon solar cell. For this experiment, the irradiance was varied between 0.1 sun and 1.2 suns, in steps of 0.1 sun. For each of these illumination intensities, the temperature was varied between 15 °C and 75 °C in steps of 5 °C. For each irradiance–temperature combination, the *I–V* curve is simulated and the V_{mpp} is determined. Subsequently, the impedance data is generated in each condition for a DC bias voltage equal to the V_{mpp}. Finally, the R_j and C_j values are obtained through CNLS analysis and are presented in Fig. 6. This is done for substrate dopant densities of 1×10^{14} cm^{-3}, 1×10^{15} cm^{-3}, and 1×10^{16} cm^{-3}.

The results in Fig. 6 show a consistent trend for all the different dopant concentration values: variations in irradiance strongly affect the maximum power point (MPP) value of both R_j and C_j, whereas the effect of temperature is limited. This outcome highlights the important role that MPPT plays in determining the operating impedance of solar cells. Whereas it was previously found that temperature has a stronger impact on the R_j-V and C_j-V relationships than illumination, the values of R_j and C_j during MPPT are more strongly affected by illumination. When the temperature increases, the reduction of the V_{mpp} approximately cancels out the enhanced diffusion effect, resulting in rather stable values of R_j and C_j. Looking at R_j specifically, the minimum and maximum MPP R_j values vary approximately between 12.9–14.4 Ω × cm^2 (1.2 suns, 75 °C) and 149–156 Ω × cm^2 (0.1 sun, 15 °C). Thus, the ranges that can be expected during practical operation are fairly similar for different bulk dopant concentrations. Shifting focus to C_j, its minimum and maximum areal MPP values show higher variability when the bulk dopant concentration is changed. For $N_{sub} = 1 \times 10^{16}$ cm^{-3}, the minimum and maximum MPP C_j values vary between 13.5 μF/cm^2 (0.1 sun, 15 °C) and 118 μF/cm^2 (1.2 suns, 75 °C). For $N_{sub} = 1 \times 10^{14}$ cm^{-3}, the variation is between 89.0 μF/cm^2 and 245 μF/cm^2. This difference confirms the important role of N_{sub} for the PN junction capacitance of solar cells. However, the MPP C_j range of $N_{sub} = 1 \times 10^{14}$ cm^{-3} and $N_{sub} = 1 \times 10^{15}$ cm^{-3} are fairly similar. This suggests that some stabilization can occur in the MPP C_j towards low dopant concentrations below 1×10^{15} cm^{-3}.

A similar analysis was conducted experimentally using the impedance spectroscopy setup. In this case, the IBC and PERC solar cell laminates were subjected to irradiance conditions between 0.1 sun and 0.5 sun in steps of 0.1 sun, whereas the temperature of the laminates was varied between 30 °C and 60 °C in steps of 10 °C. The resulting CNLS-fitted R_j and C_j values at MPP are presented in Fig. 7. The experimental results from Fig. 7 mostly confirm the observed trends from the TCAD simulations. Here too, the irradiance has stronger impact on the MPP impedance than the temperature. Notably, the experimentally observed MPP R_j ranges of the IBC and PERC laminates are highly similar to each other, as well as to that of the TCAD-simulated TOPCon device. Specifically, the MPP R_j values of the IBC cell vary between 27.8 Ω × cm^2 and 157 Ω × cm^2, whereas those of the PERC cell vary between 27.1 Ω × cm^2 and 153 Ω × cm^2. This suggests that the slope of the *I–V* curve at V_{mpp} depends significantly more on the irradiance than on the cell architecture. Conversely, the experimental results show that the MPP C_j range can be highly variable for different solar cells. As mentioned in the introduction, the MPP C_j ranges of these PERC and IBC laminates are expected to be around the lower and upper limits that can be anticipated from modern commercial c-Si solar cells, respectively. Specifically, the MPP C_j values of the IBC cell vary between 20.2 μF/cm^2 and 61.6 μF/cm^2, whereas those of the PERC cell vary between 0.283 and 1.98 μF/cm^2. Remarkably, the minimum MPP C_j value of the IBC cell is a factor ~10.2 higher than the maximum

value of the PERC cell. Additionally, the maximum MPP C_j value of the IBC cell is a factor ~218 higher than the minimum value of the PERC cell.

5. Conclusion

Various publications have emerged where the impedance of solar cells is exploited to realize innovative applications. However, for the continued advancement of such applications, it is crucial to understand how the impedance of modern solar cells varies during operation. This work reports how the PN junction impedance of modern solar cells varies across different bias voltages and under varying illumination and temperature conditions.

For a given solar cell bias voltage, variations in temperature have a notably stronger impact on the PN junction impedance than changes in irradiance. Considering that the impedance of a PN junction can be represented by a parallel resistor–capacitor (R_j-C_j) circuit, higher temperatures enhance the diffusion of minority carriers, thereby reducing R_j and increasing C_j at a given voltage, especially under high forward bias. However, during maximum power point (MPP) tracking, variations in irradiance have a greater impact on the PN junction impedance than temperature variations. This is related to the fact that increased irradiance intensity raises the MPP voltage. In contrast, when the temperature varies, the change in the diffusion process is approximately compensated by a changing MPP voltage. The range in which the MPP R_j varies was similar for different cell architectures, despite their different properties. For the performed experiment under irradiance levels between 0.1 sun and 0.5 sun and operating temperature between 30 °C and 60 °C, the MPP R_j values of the IBC cell vary between 27.8 Ω × cm^2 and 157 Ω × cm^2, whereas those of the PERC cell vary between 27.1 Ω × cm^2 and 153 Ω × cm^2. A similar range was observed for the TCAD-simulated TOPCon devices. Conversely, the range in which the MPP C_j varies is significantly affected by the substrate dopant concentration (N_{sub}) and maximum power point voltage. Specifically, the areal MPP C_j values of the IBC cell with $N_{\text{sub}} = 1.0 \times 10^{14}$ cm^{-3} varied between 20.2 μF/cm^2 and 61.6 μF/cm^2, whereas those of the PERC cell with $N_{\text{sub}} = 8.0 \times 10^{15}$ cm^{-3}varied between 0.283 and 1.98 μF/cm^2. Moreover, TCAD simulations of a performance-limit TOPCon cell with $N_{\text{sub}} = 1.0 \times 10^{14}$ cm^{-3}, where the irradiance level was varied between 0.1 sun and 1.2 suns and the operating temperature between 15 °C and 75 °C, show that the areal MPP C_j can increase to a range between 89.0 μF/cm^2 and 245 μF/cm^2.

The primary contribution of this study is to enhance the understanding of how the MPP capacitance and MPP diffusion resistance vary during solar cell operation. To achieve this, the influence of factors like illumination, temperature, and voltage is examined. The analysis is relevant for applications such as the design of MPPT circuits, visible light communication, and leveraging solar cell self-capacitance for voltage balancing in converters or power balancing among cells.

CRediT authorship contribution statement

David A. van Nijen: Writing – review & editing, Writing – original draft, Visualization, Validation, Software, Project administration, Methodology, Investigation, Formal analysis, Data curation, Conceptualization. **Salem Naoom:** Visualization, Validation, Investigation, Formal analysis, Data curation. **Mirco Muttillo:** Writing – review & editing, Validation, Software, Methodology. **Paul Procel:** Methodology. **Miro Zeman:** Funding acquisition. **Olindo Isabella:** Writing – review & editing, Supervision, Funding acquisition. **Patrizio Manganiello:** Writing – review & editing, Supervision, Software, Project administration, Methodology, Formal analysis, Conceptualization.

Declaration of Generative AI and AI-assisted technologies in the writing process

During the preparation of this work the author(s) used ChatGPT in order to improve the text flow. After using this tool/service, the author(s) reviewed and edited the content as needed and take(s) full responsibility for the content of the published article.

Declaration of competing interest

The authors declare that they have no known competing financial interests or personal relationships that could have appeared to influence the work reported in this paper.

Acknowledgments

This work is supported by the sector plan of the Dutch government in photovoltatronics research. The authors thank Rik Van Dyck for his assistance in fabricating the PERC solar cell laminate, and for characterizing the STC parameters. Furthermore, the authors thank Stefaan Heirman and Shuang Hao for their contributions to the experimental setup and the measurements.

Appendix A. Setup

A schematic representation of the setup is shown in Fig. 8.

Appendix B. PN junction capacitance theory

The depletion layer capacitance (C_{dep}) typically dominates C_j at reverse bias and at low forward bias voltage. For a PN junction consisting of homogeneously doped regions, C_{dep} is given by [39]:

$$C_{\text{dep}} = A\sqrt{\frac{q\epsilon_s N_a N_d}{2\left(V_{bi}+V_R\right)\left(N_a+N_d\right)}} \tag{5}$$

where A is the cross-sectional area of the PN junction, q is the elementary charge constant, ϵ_s is the permittivity of the semiconductor, N_a and N_d are the acceptor and donor concentrations, respectively. V_{bi} is the built-in potential, and V_R is the applied reverse-bias voltage. The low-frequency diffusion capacitance (C_{dif}) typically dominates C_j at high forward bias voltage. For a PN junction consisting of homogeneously doped regions, C_{dif} is given by [39]:

$$C_{\text{dif}} = \frac{q^2 n_i^2 A}{2kT}\left(\frac{\sqrt{D_p\tau_{p0}}}{N_d}+\frac{\sqrt{D_n\tau_{n0}}}{N_a}\right)\exp\left(\frac{qV_F}{kT}\right) \tag{6}$$

where n_i is the intrinsic carrier concentration, k is the Boltzmann constant, T is the temperature, D_p and D_n are the diffusion constant of holes and electrons. τ_{p0} and τ_{n0} are the minority charge carrier lifetimes of holes and electrons, and V_F is the applied forward-bias voltage.

Appendix C. Nyquist plots

Fig. 9 shows the Nyquist spectra that correspond to the impedance data in Fig. 2. All spectra appear to correspond to a single semicircle, representing the RC-loop of the PN junction. At 650 mV, the diameter of the semicircle is relatively small, making the inductive tail more pronounced. However, the zoomed-in view of Fig. 9(b) at 400 mV shows how the high-frequency relaxation of R_j and C_j manifests in the Nyquist spectrum. This is also referred to as the Warburg part of the impedance [1,44].

Moreover, Fig. 10 shows the Nyquist spectra of the different cells at the maximum power point, corresponding to the impedance data in Fig. 3. Within the tested frequency range, the employed small-signal circuit provides satisfactory fits.

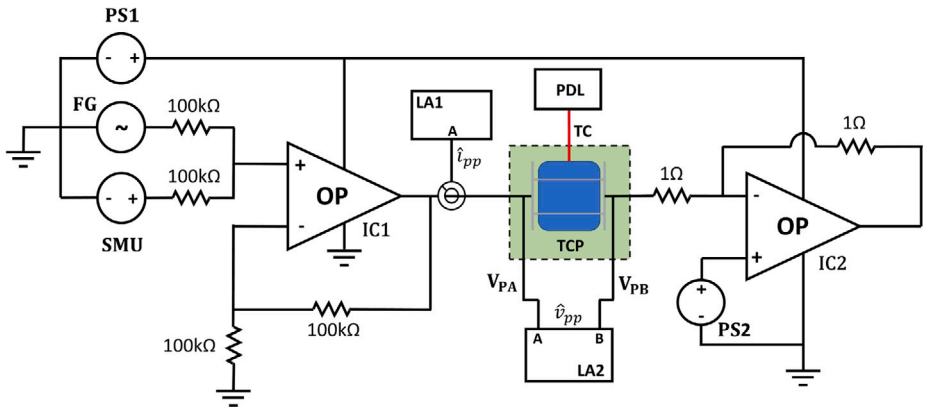


Fig. 8. Schematic representation of the employed impedance spectroscopy setup. The function generator (FG) is an Agilent 33250 A. Moreover, the opamps (OP) are of the type OPA-549 and are connected in a non-inverting summing configuration (IC1) and inverting current to voltage (transimpedance amplifier) configuration (IC2). The power supply 1 (PS1) is of the type EA-OS 2042–20. Alternatively, the power supply 2 (PS2) is a voltage divider circuit located on a printed circuit board, supplying half the voltage of PS1. This approach enables the use of a single physical power supply and prevents a high forward current to the power supply. The source measurement unit (SMU) is used to set the bias voltage. The current probe (CP) is an Yokogawa 702916 connected to channel A of the EG&G Instruments 7260 DSP lock-in amplifier (LA1). Furthermore, the voltage probes (VPA) and (VPB) are connected to the positive and negative contacts of the PV cell, respectively. On the other side, VPA and VPB are connected to channel A and B of the Signal Recovery 7225 DSP lock-in amplifier (LA2). The temperature-controlled plate (TCP) is of the type Thermo Scientific Polar Series Accel 500 LC. Finally, the temperature is monitored using a type RS pro type *T* thermocouple (TC) and a Pico TC-08 Data Logger (PDL). Setting the DC bias voltage on the PV cell, performing frequency sweeps with the function generator, and recording the values from the lock-in amplifier were done through an in-house developed Labview program.

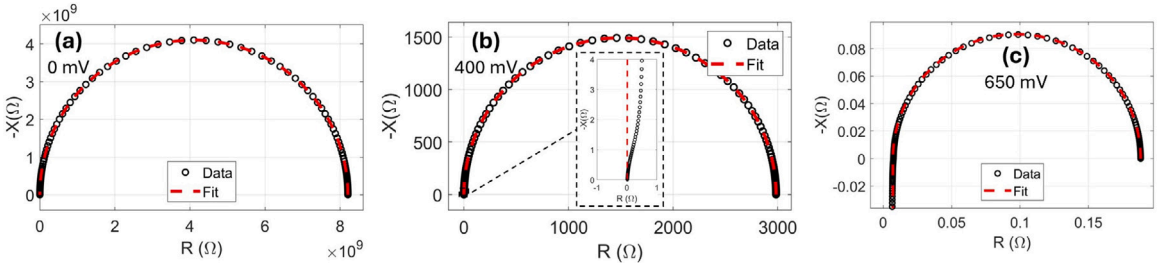


Fig. 9. TCAD-generated Nyquist spectra of TOPCon solar cell in dark conditions, along with best CNLS fits at (a) 0 mV bias, (b) 400 mV bias, and (c) 650 mV bias. These Nyquist spectra correspond to the impedance presented in Fig. 2.

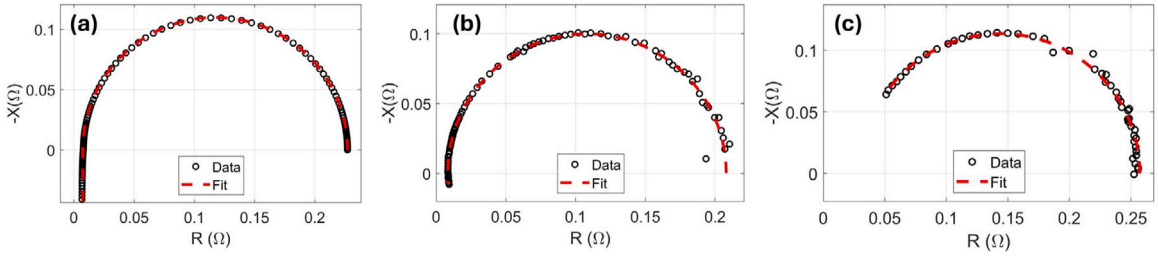


Fig. 10. Nyquist spectra at the maximum power point voltage under an irradiance of 0.5 suns, along with best CNLS fits for (a) the TCAD-generated impedance data of the TOPCon device, (b) the experimentally recorded impedance data of the IBC solar cell laminate, and (c) the experimentally recorded impedance data of the PERC solar cell laminate. These Nyquist spectra correspond to the impedance presented in Fig. 3.

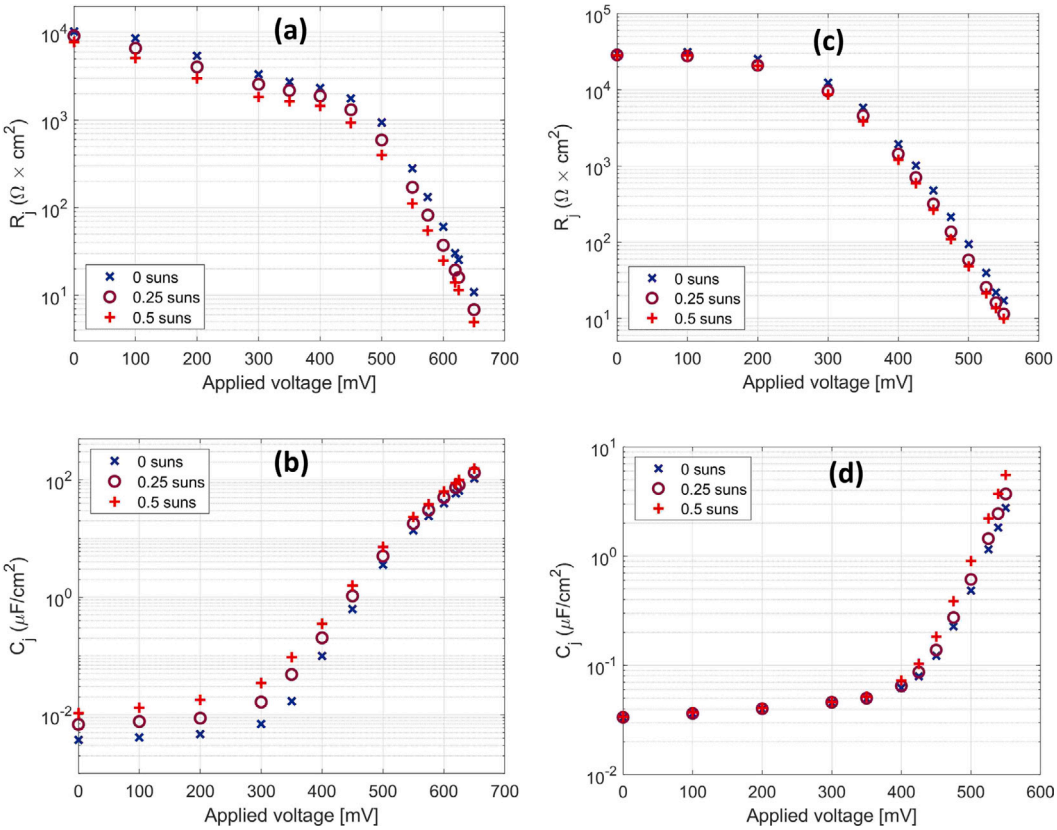


Fig. 11. Effect of illumination on R_j and C_j, as extracted through CNLS analysis from experimentally recorded impedance data of the (a–b) IBC and (c–d) PERC solar cell laminate. The irradiance is varied between dark conditions and 0.5 sun, while the temperature is kept constant at T = 30 °C.

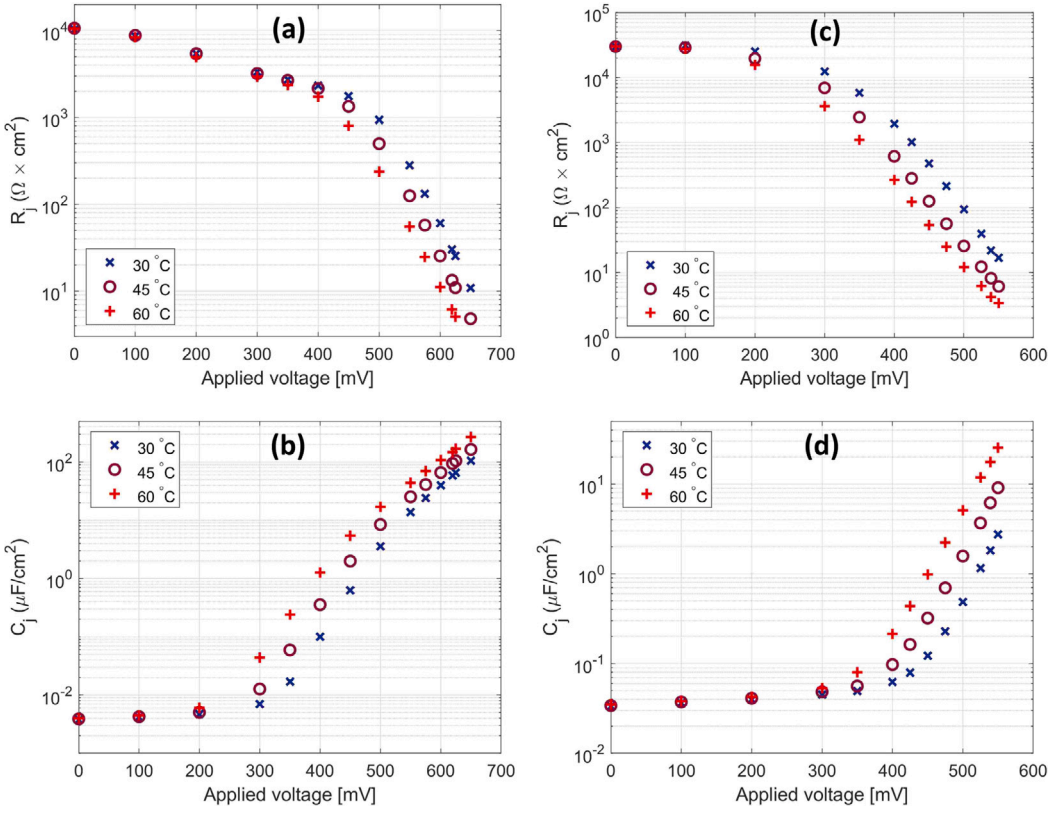


Fig. 12. Effect of temperature on R_j and C_j, as extracted through CNLS analysis from experimentally recorded impedance data of the (a–b) IBC and (c–d) PERC solar cell laminate. Temperature is varied between 30 °C and 60 °C, while the laminates are kept in dark conditions.

Appendix D. Experimental impedance results

The effect of illumination on the PN junction impedance of the single-cell laminates is shown in Fig. 11.

The effect of temperature on the PN junction impedance of the single-cell laminates is shown in Fig. 12.

Data availability

The dataset underlying this article will be made available in the 4TU ResearchData Archive, and can be accessed via the following link: https://doi.org/10.4121/5b387cd1-9b99-4042-a7b5-e92f5ad198a4.

References

[1] I. Mora-Seró, G. Garcia-Belmonte, P.P. Boix, M.A. Vázquez, J. Bisquert, Impedance spectroscopy characterisation of highly efficient silicon solar cells under different light illumination intensities, Energy Environ. Sci. 2 (2009) 678–686.

[2] J.E. Garland, D.J. Crain, J.P. Zheng, C.M. Sulyma, D. Roy, Electro-analytical characterization of photovoltaic cells by combining voltammetry and impedance spectroscopy: voltage dependent parameters of a silicon solar cell under controlled illumination and temperature, Energy Environ. Sci. 4 (2011) 485–498.

[3] I. Mora-Seró, Y. Luo, G. Garcia-Belmonte, J. Bisquert, D. Muñoz, C. Voz, J. Puigdollers, R. Alcubilla, Recombination rates in heterojunction silicon solar cells analyzed by impedance spectroscopy at forward bias and under illumination, Sol. Energy Mater. Sol. Cells 92 (2008) 505–509.

[4] J. Panigrahi, Vandana, R. Singh, N. Batra, J. Gope, M. Sharma, P. Pathi, S. Srivastava, C. Rauthan, P. Singh, Impedance spectroscopy of crystalline silicon solar cell: Observation of negative capacitance, Sol. Energy 136 (2016) 412–420.

[5] D.A. van Nijen, P. Manganiello, M. Zeman, O. Isabella, Exploring the benefits, challenges, and feasibility of integrating power electronics into c-Si solar cells, Cell Rep. Phys. Sci. 3 (2022) 100944.

[6] J.-H. Huang, B. Lehman, T. Qian, Submodule integrated boost DC-DC converters with no external input capacitor or input inductor for low power photovoltaic applications, in: 2016 IEEE Energy Conversion Congress and Exposition, ECCE, 2016, pp. 1–7, http://dx.doi.org/10.1109/ECCE.2016.7855476.

[7] A.H. Chang, A.-T. Avestruz, S.B. Leeb, Capacitor-less photovoltaic cell-level power balancing using diffusion charge redistribution, IEEE Trans. Power Electron. 30 (2015) 537–546.

[8] H. Ziar, P. Manganiello, O. Isabella, M. Zeman, Photovoltatronics: intelligent PV-based devices for energy and information applications, Energy Environ. Sci. 14 (2021) 106–126.

[9] S.-M. Kim, J.-S. Won, S.-H. Nahm, Simultaneous reception of solar power and visible light communication using a solar cell, Opt. Eng., Bellingham 53 (2014) 046103.

[10] R. Sarwar, B. Sun, M. Kong, T. Ali, C. Yu, B. Cong, J. Xu, Visible light communication using a solar-panel receiver, in: 2017 16th International Conference on Optical Communications and Networks, ICOCN, 2017, pp. 1–3, http://dx.doi.org/10.1109/ICOCN.2017.8121577.

[11] Y. Zhou, A. Ibrahim, M. Muttillo, P. Manganiello, H. Ziar, O. Isabella, Bandwidth characterization of c-si solar cells as VLC receiver under colored LEDs, in: 2023 8th International Conference on Smart and Sustainable Technologies (SpliTech), 2023, pp. 1–5, http://dx.doi.org/10.23919/SpliTech58164.2023.10193624.

[12] M. Pravettoni, D. Poh, J.P. Singh, J.W. Ho, K. Nakayashiki, The effect of capacitance on high-efficiency photovoltaic modules: a review of testing methods and related uncertainties, J. Phys. D: Appl. Phys. 54 (2021) 193001.

[13] M. Suresh, Measurement of solar cell parameters using impedance spectroscopy, Sol. Energy Mater. Sol. Cells 43 (1996) 21–28.

[14] R.A. Kumar, M.S. Suresh, J. Nagaraju, Facility to measure solar cell ac parameters using an impedance spectroscopy technique, Rev. Sci. Instrum. 72 (2001) 3422–3426.

[15] R. Kumar, M. Suresh, J. Nagaraju, Silicon (BSFR) solar cell AC parameters at different temperatures, Sol. Energy Mater. Sol. Cells 85 (2005) 397–406.

[16] S. Kumar, P. Singh, G. Chilana, Study of silicon solar cell at different intensities of illumination and wavelengths using impedance spectroscopy, Sol. Energy Mater. Sol. Cells 93 (2009) 1881–1884.

[17] D.J. Crain, J.E. Garland, S.E. Rock, D. Roy, Quantitative characterization of silicon solar cells in the electro-analytical approach: Combined measurements of temperature and voltage dependent electrical parameters, Anal. Methods 4 (2012) 106–117.

[18] P. Yadav, B. Tripathi, K. Pandey, M. Kumar, Investigating the charge transport kinetics in poly-crystalline silicon solar cells for low-concentration illumination by impedance spectroscopy, Sol. Energy Mater. Sol. Cells 133 (2015) 105–112.

[19] P. Yadav, K. Pandey, V. Bhatt, M. Kumar, J. Kim, Critical aspects of impedance spectroscopy in silicon solar cell characterization: A review, Renew. Sustain. Energy Rev. 76 (2017) 1562–1578.

[20] A. Blank, N. Suhareva, Admittance spectra of silicon photocells in dark mode, Sensors Actuators A 331 (2021) 112909.

[21] M.M. Shehata, T.N. Truong, R. Basnet, H.T. Nguyen, D.H. Macdonald, L.E. Black, Impedance spectroscopy characterization of c-Si solar cells with SiO_x/ Poly-Si rear passivating contacts, Sol. Energy Mater. Sol. Cells 251 (2023) 112167.

[22] J. Panigrahi, A. Pandey, S. Bhattacharya, A. Pal, S. Mandal, V. Krishna Komarala, Impedance spectroscopy of amorphous/crystalline silicon heterojunction solar cells under dark and illumination, Sol. Energy 259 (2023) 165–173.

[23] K. Aimaganbetov, D. Yerezhep, M. Kishkenebayev, N. Chuchvaga, N. Almas, S. Tokmoldin, N. Tokmoldin, Characterization of a heterojunction silicon solar cell by means of impedance spectroscopy, Micromachines 15 (2024).

[24] O.I. Olayiwola, P.S. Barendse, Characterization of Silicon-Based Photovoltaic Cells Using Broadband Impedance Spectroscopy, IEEE Trans. Ind. Appl. 54 (2018) 6309–6319.

[25] T. Yeow, J. Sun, Z. Yao, J.-N. Jaubert, K.P. Musselman, Evaluation of impedance spectroscopy as a tool to characterize degradation mechanisms in silicon photovoltaics, Sol. Energy 184 (2019) 52–58.

[26] O.I. Olayiwola, P.S. Barendse, Photovoltaic cell/module equivalent electric circuit modeling using impedance spectroscopy, IEEE Trans. Ind. Appl. 56 (2020) 1690–1701.

[27] R.A. Guejia-Burbano, G. Petrone, M. Piliougine, Impedance spectroscopy for diagnosis of photovoltaic modules under outdoor conditions, IEEE J. Photovolt. 12 (2022) 1503–1512.

[28] C. Pavón-Vargas, R.A. Guejia-Burbano, L.E. Garcia-Marrero, G. Petrone, Impedance spectroscopy for partial shading detection on series-connected pv panels, in: 2024 International Symposium on Power Electronics, Electrical Drives, Automation and Motion, SPEEDAM, 2024, pp. 762–767, http://dx.doi.org/10.1109/SPEEDAM61530.2024.10609152.

[29] K.C. Fong, K.R. McIntosh, A.W. Blakers, Accurate series resistance measurement of solar cells, Progr. Photovolt.: Res. Appl. 21 (2013) 490–499.

[30] R. Groves, D. Harame, D. Jadus, Temperature dependence of Q and inductance in spiral inductors fabricated in a silicon-germanium/BiCMOS technology, IEEE J. Solid-State Circuits 32 (1997) 1455–1459.

[31] N. Doumit, B. Danoumbé, S. Capraro, J.-P. Chatelon, M.-F. Blanc-Mignon, J.-J. Rousseau, Temperature impact on inductance and resistance values of a coreless inductor (Cu/Al2O3), Microelectron. Reliabil. 72 (2017) 30–33.

[32] D.A. van Nijen, M. Muttillo, R. Van Dyck, J. Poortmans, M. Zeman, O. Isabella, P. Manganiello, Revealing capacitive and inductive effects in modern industrial c-si photovoltaic cells through impedance spectroscopy, Solar Energy Mater. Solar Cells 260 (2023) 112486.

[33] P.V. tools, LOANA Solar Cell Analysis System, 2022, http://www.pv-tools.de/products/loana-system/loana-start.html, Last accessed on 21-12-2022.

[34] Synopsis, Sentaurus device user, 2021.

[35] VDMA, International technology roadmap for photovoltaics (ITRPV), 2024.

[36] A. Ingenito, G. Limodio, P. Procel, G. Yang, H. Dijkslag, O. Isabella, M. Zeman, Silicon solar cell architecture with front selective and rear full area ion-implanted passivating contacts, Solar RRL 1 (2017) 1700040.

[37] P. Procel, G. Yang, O. Isabella, M. Zeman, Numerical simulations of IBC solar cells based on poly-si carrier-selective passivating contacts, IEEE J. Photovolt. 9 (2019) 374–384.

[38] O. Breitenstein, J.P. Rakotoniaina, M.H. Al Rifai, M. Werner, Shunt types in crystalline silicon solar cells, Prog. Photovolt., Res. Appl. 12 (2004) 529–538.

[39] D.A. Neamen, Semiconductor Physics and Devices, fourth ed., McGraw Hill Education, 2012.

[40] B.A. Boukamp, A nonlinear least squares fit procedure for analysis of immittance data of electrochemical systems, Solid State Ion. 20 (1986) 31–44.

[41] D.A. van Nijen, P. Procel, R.A.C.M.M. van Swaaij, M. Zeman, O. Isabella, P. Manganiello, The nature of silicon PN junction impedance at high frequency, 2024, https://arxiv.org/abs/2409.06749. arXiv:2409.06749.

[42] W. Berry, Photovoltaic short-circuit minority carrier injection, Appl. Phys. Lett. 25 (1974) 195–196.

[43] A.R. Moore, Short-circuit capacitance of illuminated solar cells, Appl. Phys. Lett. 27 (1975) 26–29.

[44] E. von Hauff, Impedance spectroscopy for emerging photovoltaics, J. Phys. Chem. C 123 (2019) 11329–11346.